JCBFM

Quantitative assessment of microvasculopathy in arcAβ mice with USPIO-enhanced gradient echo MRI

Jan Klohs[1,2,*], Andreas Deistung[3,*], Giovanna D Ielacqua[1],
Aline Seuwen[1], Diana Kindler[1], Ferdinand Schweser[4,5],
Markus Vaas[1,2], Anja Kipar[6], Jürgen R Reichenbach[3,7,8,9] and
Markus Rudin[1,2,10]

Abstract
Magnetic resonance imaging employing administration of iron oxide-based contrast agents is widely used to visualize cellular and molecular processes in vivo. In this study, we investigated the ability of R_2^* and quantitative susceptibility mapping to quantitatively assess the accumulation of ultrasmall superparamagnetic iron oxide (USPIO) particles in the arcAβ mouse model of cerebral amyloidosis. Gradient-echo data of mouse brains were acquired at 9.4 T after injection of USPIO. Focal areas with increased magnetic susceptibility and R_2^* values were discernible across several brain regions in 12-month-old arcAβ compared to 6-month-old arcAβ mice and to non-transgenic littermates, indicating accumulation of particles after USPIO injection. This was concomitant with higher R_2^* and increased magnetic susceptibility differences relative to cerebrospinal fluid measured in USPIO-injected compared to non-USPIO-injected 12-month-old arcAβ mice. No differences in R_2^* and magnetic susceptibility were detected in USPIO-injected compared to non-injected 12-month-old non-transgenic littermates. Histological analysis confirmed focal uptake of USPIO particles in perivascular macrophages adjacent to small caliber cerebral vessels with radii of 2–8 μm that showed no cerebral amyloid angiopathy. USPIO-enhanced R_2^* and quantitative susceptibility mapping constitute quantitative tools to monitor such functional microvasculopathies.

[1]Institute for Biomedical Engineering, ETH & University of Zurich, Zurich, Switzerland
[2]Neuroscience Center Zurich, University of Zurich and ETH Zurich, Zurich, Switzerland
[3]Medical Physics Group, Institute of Diagnostic and Interventional Radiology, Jena University Hospital–Friedrich Schiller University Jena, Jena, Germany
[4]Buffalo Neuroimaging Analysis Center, Department of Neurology, School of Medicine and Biomedical Sciences, State University of New York at Buffalo, Buffalo, NY, USA
[5]MRI Clinical and Translational Research Center, School of Medicine and Biomedical Sciences, State University of New York at Buffalo, Buffalo, NY, USA
[6]Laboratory for Animal Model Pathology, Institute of Veterinary Pathology, Vetsuisse Faculty, University of Zurich, Zurich, Switzerland

[7]Abbe School of Photonics, Friedrich Schiller University Jena, Jena, Germany
[8]Center of Medical Optics and Photonics, Friedrich Schiller University Jena, Jena, Germany
[9]Michael Stifel Center for Data-driven and Simulation Science Jena, Friedrich Schiller University Jena, Jena, Germany
[10]Institute of Pharmacology and Toxicology, University of Zurich, Zurich, Switzerland
*The first two authors contributed equally to this work.

Corresponding author:
Jan Klohs, Institute for Biomedical Engineering, University of Zurich and ETH, AIC–ETH HCI D426 Vladimir-Prelog-Weg 4, CH-8093 Zurich, Switzerland.
Email: klohs@biomed.ee.ethz.ch

Introduction

Over the past several years, there has been an increasing interest and effort in developing magnetic resonance imaging (MRI) assays to visualize cellular and molecular processes in vivo. To this end, iron oxide particle-based contrast agents like superparamagnetic iron oxide (SPIO) or ultrasmall superparamagnetic iron oxide (USPIO) nanoparticles have been used.[1] Cellular MRI is performed either by intravenous injection of iron oxide nanoparticles, which are subsequently taken up by phagocytic cells, or by adoptively transferring cells, which have been exogenously labeled with the nanoparticles. Iron oxide particle-based contrast agents increase the transverse relaxation rate by an amount $\Delta R_{2,CA}$ and alter the local magnetic susceptibility ($\Delta\chi_{CA}$), which enhances the reversible fraction to the transverse relaxation rate by $\Delta R_{2',CA}$ and thereby signal dephasing. Thus, the local effective transverse relaxation rate $R_{2,CA}^*$ of a contrast agent experiment extracted from a gradient echo (GRE) experiment is given by the sum of intrinsic contributions from the native tissue ($R_{2,i}^*$) and the contrast agent ($\Delta R_{2,CA}^*$), i.e., $R_{2,CA}^* = R_{2,i}^* + \Delta R_{2,CA}^* = R_{2,i}^* + \Delta R_{2,CA} + \Delta R_{2',CA}$, and depends sensitively on the presence of iron particles due to their high intrinsic transverse relaxivity. Consequently, voxels that contain cells with ingested iron particles are displayed with reduced intensity (hypointense) on T_2- or T_2^*-weighted images.

Several MRI methods have been developed for quantification of iron oxide-based contrast agents. One common approach is relaxometry, i.e., the analysis of the magnitude signal decay to extract transverse relaxation rates $R_{2,CA}$ or effective transverse relaxation rates $R_{2,CA}^*$ of iron oxide particles in the tissue.[2,3] Although many reports have demonstrated a linear relationship between $R_{2,CA}$ or $R_{2,CA}^*$ and iron concentration,[4,5] there are additional variables that influence relaxation, such as size, intravoxel distribution and compartmentalization of the particles, or changes in the composition of the surrounding tissue.[3,5,6] Thus, relaxometric procedures may misestimate iron concentrations. Alternatively, phase information obtained from GRE data can be used for quantitative analysis of iron content since iron oxide nanoparticles give rise to local changes of magnetic susceptibility, which are detected as changes in signal phase.[7–9] However, direct correlation between phase and iron content is impeded due to the non-local relationship between an arbitrary magnetic susceptibility distribution and its effect on the resulting magnetic field.[10] Therefore, iron quantification based solely on phase is only reliable if the distribution of iron oxide particles is of a simple, geometrically regular shape, such as a sphere.[9]

Quantitative susceptibility mapping (QSM), a recently introduced post-processing technique for GRE phase information, promises to overcome this limitation. QSM converts phase images into maps of bulk magnetic susceptibility distribution, which can be analyzed directly.[11–13] The benefit of QSM in quantifying the amount of iron oxide nanoparticles in biological tissue has recently been demonstrated for nanoparticles injected into skeletal muscle ex vivo,[14] as well as in vivo with nanoparticles that had been functionalized against the intercellular adhesion molecule-1 in a lipopolysaccharide-induced model of acute inflammation.[15]

In the present work, we demonstrate the feasibility of QSM to visualize and quantify USPIO accumulation in the brain of arcAβ mice at 9.4 T. The arcAβ mouse strain is a genetic model of cerebral amyloidosis and exhibits progressive accumulation of amyloid-β (Aβ) protein in brain parenchyma and in the walls of cerebral vessels (cerebral amyloid angiopathy, CAA) with pronounced vascular remodeling.[16–18] Hence, the strain is well suited to serve as a model of hereditary cerebral hemorrhage with amyloidosis,[19] and Alzheimer's disease.[20] We evaluated the visibility of USPIO accumulation on quantitative susceptibility and R_2^* maps and quantified iron particle deposition by measuring changes in R_2^* and magnetic susceptibility. Histological analysis was performed to investigate vasculopathy and demonstrate the cellular uptake of USPIOs in situ.

Materials and methods

Animals

All experimental procedures conformed to the national guidelines of the Swiss Federal Act on Animal Protection and were approved by an official committee (license 194/2011, Cantonal Veterinary Office, Zurich, Switzerland). We confirm compliance with the ARRIVE guidelines on reporting animal experiments. Transgenic (arcAβ) mice and non-transgenic littermates (NTL) of either sex were used. Animals were kept at standard housing conditions with a 12-h dark/light cycle and were provided with water and food ad libitum.

USPIO

P904 (Guerbet, France) is an USPIO and consists of an iron oxide core and a hydrophilic coating of a monomeric organic molecule with 20 hydroxylic groups, resulting in a mean hydrodynamic diameter of 21 nm.[21] P904 is cleared from the blood with a rate of 0.73 mL/min/kg.[22] As P904 is less prone to liver uptake compared to SPIO its blood half-life and thus its uptake capacity by macrophages is increased.[23] The

P904 that is taken up by macrophages has been found to be degraded to non-toxic ferritin.[24]

Magnetic resonance imaging

The study was performed using four batches of animals: The first batch consisted of six arcAβ mice and six NTL of 5.8–6.5 months of age and was assessed with MRI without USPIO injection. The second batch consisted of five arcAβ mice and six NTLs of 6–6.7 months of age and comprised animals from the first batch that were, after one week of recovery, assessed with MRI a second time 18 h after intravenous injection of P904 (1000 μmol/kg body weight). The third batch consisted of 11 arcAβ mice and 12 NTL of 9.6–12.2 months of age that were measured with MRI without USPIO injection. The fourth batch of mice consisted of 11 arcAβ mice and 7 NTL of 11.5–12.5 months of age which were assessed with MRI 18 h after intravenous injection of P904.

MRI data were acquired on a Bruker BioSpec 94/30 (Bruker BioSpin GmbH, Germany) small animal MR system operating at 9.4 T. The system was equipped with a cryogenic receive only 2×2 phased-array mouse head surface coil (Bruker BioSpin AG, Fällanden, Switzerland). A linearly polarized volume resonator was used for homogeneous transmission. Anesthesia was induced with 3 % isoflurane (Abbott, Cham, Switzerland) in a 4:1 air/oxygen mixture. The mice were endotracheally intubated and mechanically ventilated during the measurements with 80 breaths/minute and a respiration cycle of 25 % inhalation and 75 % exhalation (MRI-1 Volume Ventilator; CWI Inc., Ardmore, USA) using 1.2 % isoflurane. Body temperature was monitored with a rectal temperature probe (MLT415, ADInstruments) and kept at $36.0 \pm 0.5°C$ using a warm-water circuit integrated into the animal support (Bruker BioSpin). Anatomical reference data acquired in coronal and sagittal orientations served for accurate positioning of the animal's head. Global first-order shimming followed by field-map-based local shimming was performed on the mouse brain using the automated MAPshim routine to reduce field inhomogeneities. A 3D multi-echo GRE sequence was applied using a field-of-view of 25.6 mm × 25.6 mm × 8 mm and an acquisition matrix of 256 × 256 × 80, resulting in an effectively isotropic spatial resolution of 100 μm × 100 μm × 100 μm. Four echoes were recorded (echo times (TE) = 3.2 ms/7.8 ms/12.4 ms/17 ms) with repetition time = 80 ms, flip angle = 15°, bandwidth = 78 kHz, monopolar echo readout, and no averaging within an acquisition time of ~20 min.

The relaxivity (r_2^*) and the molar susceptibility of P904 at a magnetic field strength of 9.4 T were determined at room temperature (T = 295 K) by measuring different contrast agent concentrations in distilled water ($c_{P904} = 0.03$ mM/0.06 mM/0.12 mM/0.24 mM/1.2 mM/2.4 mM). The different aqueous solutions were guided through a tube that was immersed into a water bath. For each P904 concentration, the experimental setup was imaged using a 3D multi-echo GRE sequence with the same geometry as for the mouse head. Six echoes were recorded (echo times (TE) = 3.0 ms/6.6 ms/10.2 ms/13.8 ms/17.4 ms/21.0 ms) with repetition time = 80 ms, flip angle = 15°, bandwidth = 78 kHz, monopolar echo readout, and no averaging.

Histology and immunohistology

Upon completion of MRI measurements, mice were transcardially perfused with phosphate-buffered saline (PBS, pH 7.4), followed by 4% buffered paraformaldehyde (PFA; pH 7.4) for fixation. Brains were removed from the skull and fixed for another 24 h, after which horizontal slices (approx. 2 mm) of the entire brain were prepared and embedded in paraffin wax. Sections (4 μm) were prepared and stained with hematoxylin-eosin (HE) for histopathological assessment and with Perls' Prussian blue for the demonstration of iron (Fe^{3+}). Briefly, slides were incubated in a 1% potassium ferrocyanide and 0.5% hydrochloric acid solution, followed by incubation with a 0.1% solution of nuclear fast red with aluminum sulfate for nuclear counterstaining. For diaminobencidine (DAB) enhancement of the Perls' Prussian blue stain, slides were washed in TBS-Tween and incubated for 15 min with Peroxidase Blocking Solution (Dako), then washed with tap water and counterstained with hemalaun for 1 s. Demonstration of iron within macrophages/microglial cells was achieved by staining with Perls' Prussian blue (blue), nuclear fast red, and immunohistology for Iba1. Consecutive sections were used for triple immunohistology, using rat anti-mouse CD31 (PECAM-1; clone SZ31, Dianova, Germany) for the demonstration of endothelial cells, rabbit anti-Iba1 (anti-peptide antibody, Wako Pure Chemicals) for the staining of microglial cells/macrophages, and mouse anti-beta amyloid (Aβ; clone 6E10, BioLegend) for the demonstration of Aβ deposition. Antigen retrieval was achieved by incubation in Retrieval-Buffer 2 (Leica AR9640) for 45 min at 100°C (CD31) and for 10 min at 95°C (Iba1). Sections were incubated for 30 min at room temperature with the primary antibodies diluted 1:200 (anti-CD31), 1:2,500 (anti-Iba1), and 1:5,000 (anti-Aβ) in Antibody Diluent (Leica AR9352) followed by incubation with rabbit anti-rat Ig (1:1,000, Abcam) and the Refine AP-Kit with new fast red as chromogen (Leica) for CD31, the Refine HRO kit and DAB as chromogen

for Iba1, and the Refine HRP-kit (Leica) and perma-blue as chromogen (Diagnostic Biosystems) for Aβ.

MRI data processing

Single-channel GRE magnitude images were combined using the sum-of-squares method,[25] whereas single-channel GRE phase images were combined by taking the argument of the complex summed single-channel images after subtracting the channel-dependent phase offset estimated in the center of the three-dimensional volume of the first echo.[26] Quantitative susceptibility maps were computed based on these combined phase images. To this end, the combined phase images for each echo were unwrapped using a 3D best-path algorithm,[27] divided by $(2\pi \cdot TE)$ to obtain the Larmor frequency variation in Hz, and then combined across the different TEs in an optimized way that takes into account the local echo-time dependent contrast-to-noise ratio of the Larmor frequency images.[28] Background frequency contributions were eliminated using sophisticated harmonic artifact removal for phase data (SHARP),[11] with 10 different spherical kernels with varying radii ranging from $100\,\mu m$ to $1000\,\mu m$,[29] employing a regularization parameter for truncated singular value decomposition of 0.05. Susceptibility mapping was performed based on SHARP-processed frequency images using homogeneity-enabled incremental dipole inversion (HEIDI).[12]

Maps of the effective transverse relaxation rate, R_2^*, were calculated from the magnitude images using the power method.[30,31] The squared magnitude signal decay $S(\vec{r}, TE)^2$ of the multi-echo GRE scan was used for the regression and the following function was fitted using the logarithmic calculus

$$S(\vec{r}, TE)^2 = S_0(\vec{r})^2 \cdot \exp(-2 \cdot TE \cdot R_2^*(\vec{r})) \qquad [1]$$

where $S_0(\vec{r})$ is the (unknown) signal intensity at $TE = 0$ and $\vec{r}$ is the position vector.

Data analysis

Generated maps were excluded from further analysis in case of artifacts (the number of analyzed maps for each group is given in Table 1). Three-dimensional volumes-of-interest (VOIs) were identified on magnitude images covering the olfactory bulb, cerebral cortex, striatum, hippocampus, thalamus, brain stem, and the ventricles using MRIcron (www.sph.sc.edu/comd/rorden/mricron/). Analysis was performed blinded with regard to the experimental group. VOIs were applied to R_2^* and susceptibility maps and mean values were calculated for each region. The maps were visually inspected and in cases of apparent artifacts (e.g., induced by insufficient

shimming) VOI values were excluded from analysis. All susceptibility values were referenced to the magnetic susceptibility measured in the ventricles. In addition, in one 12-month-old arcAβ mouse with and one mouse without P904 injection VOIs were manually defined in 10 cortical vessels to estimate the amount of iron uptake. These vessels were identified based on their increased intensity on magnetic susceptibility maps and their tubular shape was assessed by following the vessel path across several adjacent slices.

Linear regression between P904 concentration (c_{P904}) and the magnetic susceptibility difference with respect to the surrounding water and between c_{P904} and the R_2^* value of the P904 solution was applied to determine the molar susceptibility and r_2^*, respectively (Supplementary Figure 1). Using the determined molar susceptibility, the measured susceptibility differences between arcAβ mice with and without P904 injection in different brain areas were converted into iron estimates as an indicator for the USPIO concentration ($c_{P904,arcA\beta}$).

Results

GRE data of 6- and 12-month-old NTL and arcAβ mice were acquired without and 18 h after intravenous injection of P904. Representative horizontal sections of R_2^* and magnetic susceptibiltiy maps are displayed in Figure 1. In NTL of both ages, non-injected and P904-injected 6-month-old arcAβ mice and non-injected 12-month-old arcAβ mice only few focal areas were discernible with increased magnetic susceptibility and R_2^* values. These areas most likely constitute venous structures with a high amount of paramagnetic deoxy-hemoglobin.[32] In the brains of 12-month-old arcAβ mice, however, a large number of foci of increased R_2^* and magnetic susceptibility were observed 18 h after P904 administration, indicating accumulation of USPIO particles. Axial sections of susceptibility maps revealed accumulation of USPIO particles in the cerebral cortex, striatum, and hippocampus (Figure 2).

To obtain a quantitative estimate of USPIO accumulation, we performed VOI analysis of susceptibility and R_2^* for different anatomical regions (Table 1). Statistical analysis was only performed for 12-month-old mice because of the small group size of 6-month-old mice. R_2^* and $\Delta\chi$ values for each genotype were compared with and without P904 injection. In NTL, there were no significant differences in R_2^* and $\Delta\chi$ for all investigated brain regions. In contrast, significantly higher R_2^* values were measured in P904-injected arcAβ mice compared to non-injected arcAβ mice in the olfactory bulb, cerebral cortex, hippocampus, striatum, and thalamus but not in the brain stem. Significantly higher magnetic susceptibility differences,

Table 1. VOI analysis of R_2^* and susceptibility maps (values of $\triangle\chi$ are given relative to the mean susceptibility in CSF).

	R_2^* (s^{-1})		$\triangle\chi$ (ppm)		$c_{P904,arcA\beta}$ (μmol/l)
	wt	arcAβ	wt	arcAβ	
6 months of age, no P904					
°Olfactory bulb	30.1 ± 0.8 (6)	29.7 ± 0.7 (6)	-0.030 ± 0.007 (6)	-0.032 ± 0.005 (6)	
°Cortex	29.7 ± 1.4 (6)	28.6 ± 0.4 (6)	-0.029 ± 0.006 (6)	-0.031 ± 0.006 (6)	
°Hippocampus	28.2 ± 1.3 (6)	27.3 ± 0.3 (6)	-0.032 ± 0.005 (6)	-0.034 ± 0.004 (6)	
°Striatum	31.0 ± 0.9 (6)	31.3 ± 0.7 (6)	-0.031 ± 0.006 (6)	-0.033 ± 0.006 (6)	
°Thalamus	33.5 ± 1.6 (5)	32.2 ± 1.0 (6)	-0.032 ± 0.006 (6)	-0.034 ± 0.005 (6)	
°Brain stem	38.3 ± 2.1 (5)	38.7 ± 2.3 (6)	-0.028 ± 0.006 (6)	-0.031 ± 0.006 (6)	
6 months of age, with P904					
°Olfactory bulb	34.2 ± 6.6 (5)	33.3 ± 5.4 (4)	-0.028 ± 0.012 (5)	-0.034 ± 0.009 (4)	–
°Cortex	33.7 ± 7.0 (5)	32.5 ± 5.5 (4)	-0.027 ± 0.012 (5)	-0.027 ± 0.011 (4)	186
°Hippocampus	30.6 ± 6.4 (5)	31.1 ± 4.0 (4)	-0.032 ± 0.010 (5)	-0.029 ± 0.009 (5)	232
°Striatum	35.7 ± 10.3 (5)	37.0 ± 7.9 (4)	-0.028 ± 0.016 (5)	-0.028 ± 0.010 (4)	232
°Thalamus	38.9 ± 11.4 (5)	38.8 ± 8.9 (4)	-0.030 ± 0.012 (5)	-0.029 ± 0.011 (4)	232
°Brain stem	42.5 ± 12.3 (5)	46.9 ± 9.1 (4)	-0.026 ± 0.014 (5)	-0.026 ± 0.012 (4)	232
12 months of age, no P904					
°Olfactory bulb	32.5 ± 1.2 (12)	31.2 ± 1.0 (9)	-0.023 ± 0.008 (12)	-0.030 ± 0.007 (10)	
°Cortex	30.1 ± 0.8 (11)	30.2 ± 1.8 (9)	-0.024 ± 0.006 (12)	-0.029 ± 0.006 (10)	
°Hippocampus	28.8 ± 1.3 (12)	28.9 ± 2.1 (9)	-0.026 ± 0.006 (12)	-0.032 ± 0.006 (10)	
°Striatum	32.2 ± 0.8 (12)	31.9 ± 0.8 (9)	-0.025 ± 0.006 (12)	-0.034 ± 0.006 (9)	
°Thalamus	33.9 ± 1.0 (12)	33.6 ± 1.4 (9)	-0.027 ± 0.006 (12)	-0.032 ± 0.006 (10)	
°Brain stem	39.8 ± 1.5 (12)	40.9 ± 2.0 (7)	-0.022 ± 0.006 (12)	-0.028 ± 0.006 (10)	
°Cortical vessels		58.1 ± 12.5 (1)		-0.002 ± 0.01 (1)	
12 months of age, with P904					
°Olfactory bulb	31.8 ± 2.1 (7)	34.1 ± 2.5 (11)*	-0.029 ± 0.004 (6)	-0.025 ± 0.008 (11)	232
°Cortex	29.0 ± 1.8 (7)	32.7 ± 3.1 (11)*	-0.029 ± 0.005 (6)	-0.023 ± 0.008 (10)*	278
°Hippocampus	27.7 ± 1.7 (7)	31.4 ± 2.2 (11)*	-0.030 ± 0.004 (6)	-0.025 ± 0.007 (11)*	325
°Striatum	33.4 ± 2.1 (7)	35.8 ± 3.6 (11)*	0.028 ± 0.004 (6)	-0.028 ± 0.004 (11)*	278
°Thalamus	33.1 ± 2.6 (7)	36.9 ± 3.1 (11)*	-0.031 ± 0.004 (7)	-0.026 ± 0.009 (10)	278
°Brain stem	38.1 ± 3.1 (7)	44.5 ± 4.6 (11)	-0.028 ± 0.005 (7)	-0.023 ± 0.007 (10)	232
°Cortical vessels		118 ± 10 (1)		0.02 ± 0.015 (1)	1020

Mean value and standard deviations of R_2^* and magnetic susceptibility $\Delta\chi$ for individual brain regions across animals. Mean values and standard deviations for cortical vessels were obtained across 10 vessels in one 12-month-old arcAβ mouse with and without P904 injection. The concentrations of P904 in arcAβ mice ($c_{P904,arcA\beta}$) were estimated based on the susceptibility differences between arcAβ mice with and without USPIO administration. The number in brackets gives the group size. * indicates statistical significant differences between P904 versus non-injected 12-month-old mice of the same genotype using Student's *t*-test ($p \leq 0.05$).

$\Delta\chi$, relative to cerebrospinal fluid were measured in the cerebral cortex, hippocampus, and striatum of injected compared to non-injected arcAβ mice, but not in the olfactory bulb, thalamus, and brain stem. As a reference for the quantitative assessment, we analyzed the P904 effect on the quantitative MRI parameters in voxels that fully covered cortical vessels of a 12-month-old arcAβ mouse with and without P904 injection (Table 1). Significantly higher R_2^* and $\Delta\chi$ values were observed after P904 administration. To transfer the estimated susceptibility differences between arcAβ mouse with and without P904 injection into USPIO concentrations (Table 1), we characterized the contrast agent at a magnetic field strength of 9.4 T in an experimental setup (Supplementary Figure 1) and determined its molar susceptibilty to be 0.0216 ppm*l/
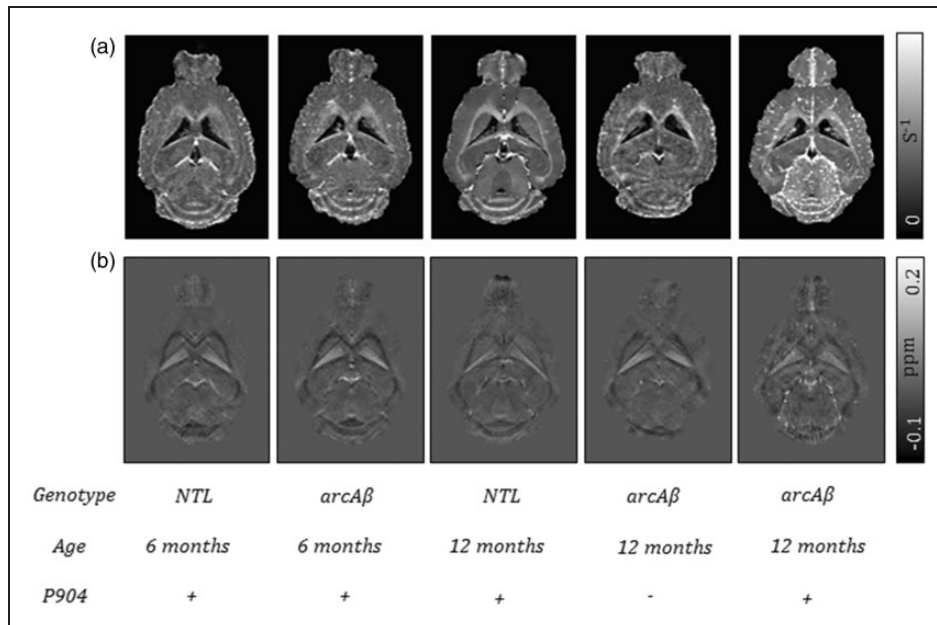
Figure 1. (a) Representative horizontal sections of R_2^* maps of 6- and 12-month-old non-transgenic littermates (NTL) and arcAβ mice. (b) Corresponding quantitative susceptibility maps. Only in the 12-month-old arcAβ mouse focal areas of R_2^* values and high magnetic susceptibility are revealed 18 h after intravenous injection of P904, indicating accumulation of P904. The + and − symbol for P904 (last column) indicates MRI with and without USPIO injection, respectively.

mmol and its r_2^* to be $84.3\,\mathrm{s}^{-1}$ * l/mmol. Our molar susceptibilitiy is substantially smaller than 2.3 ppm * l/mmol measured by Wang et al.[33] at a magnetic field strength of 2.35 T and may be explained by a non-linear relationship between the magnetization of the USPIO and the applied magnetic field strength.

Histological analysis was used to investigate vasculopathy and cellular uptake of USPIOs. This analysis did neither reveal pathological changes in the 6-month-old arcAβ mice nor in the NTL. However, in all 6-month-old arcAβ mice, small caliber vessels occasionally exhibited a variable degree of vascular Aβ deposition, ranging from very small granular over larger patchy to circular deposits, but showed no parenchymal Aβ deposition (Figure 3(a)). Cerebral vessels were not associated with the presence of activated perivascular macrophages and there was no evidence of iron uptake.

The brains of both USPIO injected and non-injected 12-month-old arcAβ mice revealed vascular changes consistent with CAA (Figure 3(c)),[17] together with multifocal parenchymal Aβ plaques with associated microgliosis (Figure 3(f)), which was most prominent in the cortex. Immunohistology identified a variable degree of vascular Aβ deposition in the walls of small caliber vessels, which was patchy or circular and often extended over a considerable length of the vessels (Figure 3(d) and (e)). Around more severely affected vessels, Aβ deposits stretched into the adjacent parenchyma, where one or occasionally several Iba1-positive

cells with the morphology of activated microglia were found (Figure 3(d) and (e)). Immunohistology also confirmed the multifocal parenchymal deposits as dense Aβ aggregates which, as previously described,[34] were surrounded by or intermingled with Iba1-positive, activated microglial cells (see Figure 3(f)). In USPIO injected mice, a few small foci were identified, in which individual small caliber vessels (radius: 2–8°μm) exhibited one or a few perivascular elongated cells that contained iron-positive material, consistent with cellular uptake of USPIOs (Figure 3(g) and (h)). Combined Perls' Prussian blue and immunohistological staining for Iba1 confirmed these cells as macrophages. However, their morphology was consistent with perivascular macrophages and not with activated microglia.[35] These vessels did not exhibit any histopathological changes, in particular there was no morphological evidence of CAA. In contrast, in CAA-affected vessels we did not detect iron-positive material. Rarely, individual iron-containing cells with the morphology of macrophages/microglial cells were also found in the parenchyma within these areas (Figure 3(g), arrows).

Discussion

GRE MRI techniques are highly sensitive to the underlying magnetic susceptibility distribution. Iron oxide-based contrast agents are used as label for cellular MR studies because they generate localized variations
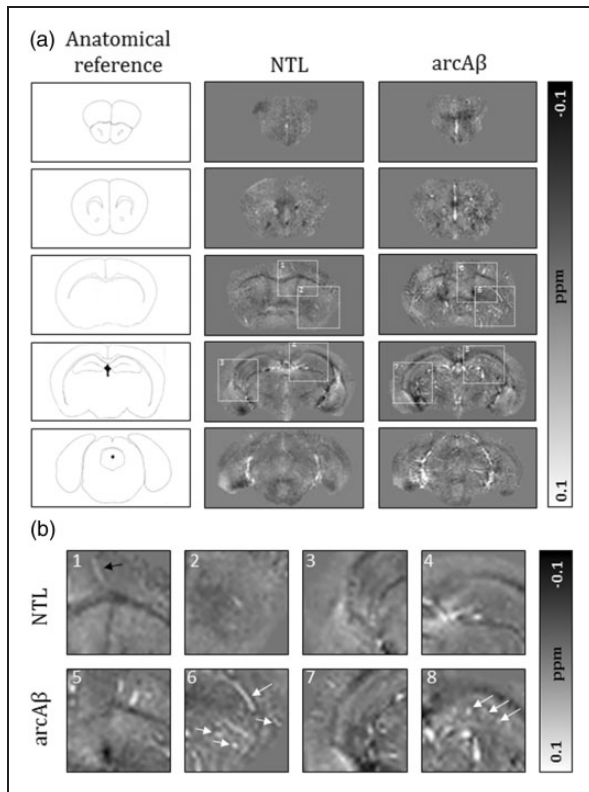
Figure 2. (a) Axial brain sections of susceptibility maps of a 12-month-old non-transgenic littermate (NTL) and an arcAβ mouse taken at different anatomical locations. The white dashed boxes indicate the anatomical region highlighted in the enlarged sections (b). (b) Enlarged images reveal areas of high susceptibility in the NTL animal, presumably veins, that contain a high amount of paramagnetic deoxyhemoglobin (black arrow). Focal areas of high susceptibility in cortical regions, the striatum, and hippocampus of the arcAβ mouse are indicative of USPIO particle accumulation in these regions (white arrows).

in magnetic susceptibility ($\Delta\chi$) and R_2 (or R_2^*) values, thereby enhancing signal dephasing. These effects are usually detected as hypointensities (negative contrast) on T_2- or T_2^*-weighted magnitude images, which however do not provide quantitative information on the amount of the accumulated contrast agent. In the current study, we demonstrated the ability of R_2^* mapping and QSM not only to visualize but also to quantify USPIO accumulation in the arcAβ model of cerebral amyloidosis. We observed nanoparticle accumulation specifically in certain brain regions of 12-month-old arcAβ mice after injection of P904 (Figures 1 and 2). Local values of tissue R_2^* were increased by 2.5 to $3.9\,s^{-1}$, and $\Delta\chi$ values were 0.004 to 0.006 ppm higher in brain regions with USPIO accumulation. Based on the measured molar susceptibility value of P904 of 0.0216 ppm/mM, we estimated that USPIO contrast agent concentration ranged from 232 to 325 μmol/l (Table 1).

Quantifying USPIO concentrations on the basis of R_2^* and susceptibility changes in vivo is, however, challenging because variations in these two parameters can be governed by a number of factors. In homogeneous solutions changes in $R_{2,CA}$ or $R_{2,CA}^*$ and magnetic susceptibility depend linearly on the iron concentration,[4,5] whereas in biological samples these changes are also influenced by intrinsic $R_{2,i}$ ($R_{2,i}^*$) and magnetic susceptibility contributions from the tissue, which might be altered by changes in the tissue microstructure, e.g., due to ageing or in the case of arcAβ mice by amyloidosis.[36] Since these effects on R_2^* and $\Delta\chi$ are unknown a priori, we acquired baseline GRE data of mice not injected with P904 to enable estimation of the effect of USPIO accumulation.

The effect of an injected iron oxide contrast agent on R_2^* and $\Delta\chi$ values will be reduced due to partial volume effects, as the volume fraction containing the contrast agent is small, e.g., perivascular macrophages at small caliber vessels compared to the voxel dimension. This might explain why the effects on R_2^* and $\Delta\chi$ values after P904 injection are relatively small. This becomes obvious when confining the analysis to VOIs comprising essentially cortical vessels only. A mean susceptibility difference of 0.022 ppm was observed in cortical vessels between a 12-month-old arcAβ mouse with and without P904 administration, which corresponds to a local P904 concentration of 1020 μmol/l. Taking into account the voxel volume of 1 nl we estimate an amount of substance of 1.02 pmol which corresponds to 57 pg of iron (molar weight of iron is 56 g/mol). This is substantially larger than the corresponding values found for a large cortical VOI, for which $\Delta\chi$ was found to be 0.005 ppm, corresponding to 15.6 pg of iron. This might still be an underestimation as the USPIOs are not distributed across the whole vessel but rather confined to the vessel wall. Obviously, such analyses are only applicable to regions in which resolved vascular structures are comparable in size with the voxel dimensions. We measured the radii of vessels to which USPIOs accumulate on Perls' Prussian blue and nuclear fast red double-stained slices to range from 2 to 8 μm, which is smaller than the typical MRI voxel size. In these cases, the affected vessels cannot be reliably identified and MRI analysis is limited to tissue VOIs.

We also found differences in the sensitivity between R_2^* mapping and QSM. While with R_2^* mapping we found significantly increased values in five brain regions, with QSM we detected an increase in $\Delta\chi$ in only three regions (Table 1). Due to non-local effects of changes in susceptibility on the magnetic field, a region experiencing enhanced signal dephasing by the presence of USPIO particles extends beyond the dimensions of the magnetic inclusion (blooming
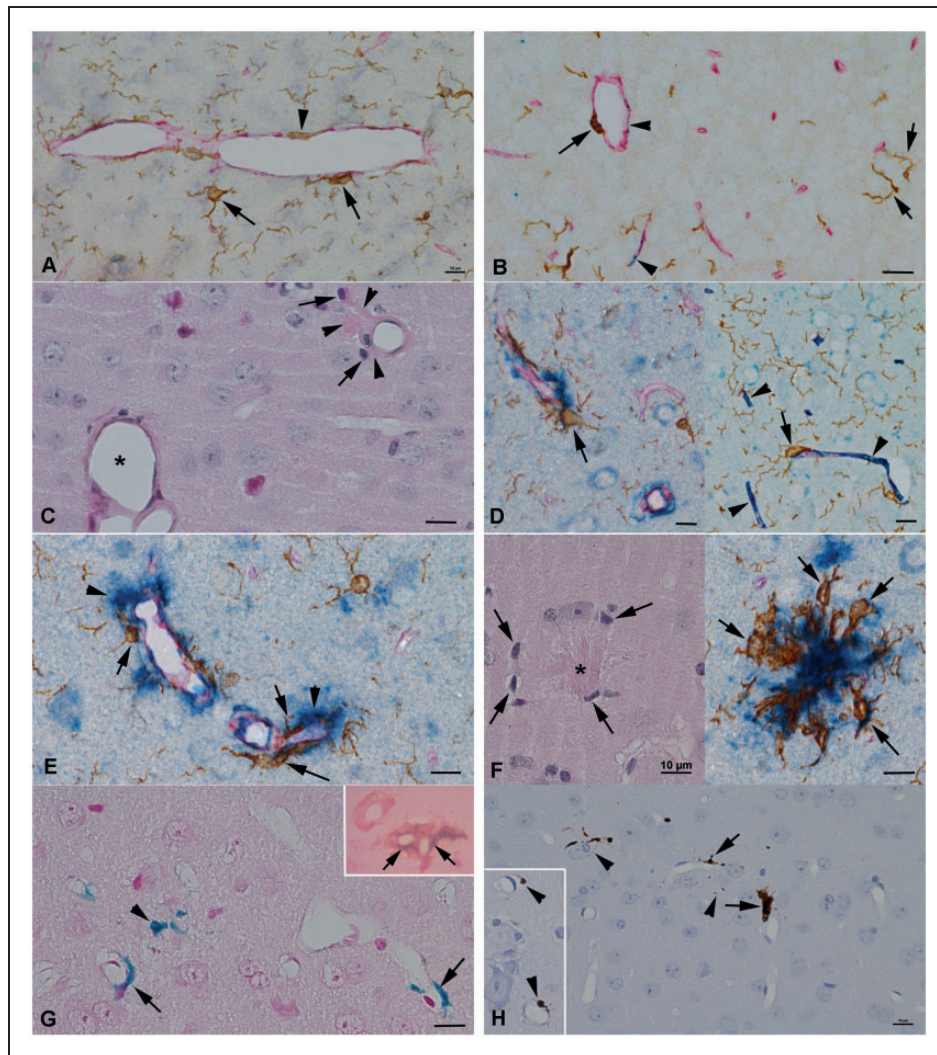
Figure 3. Histological findings in the cortex of arcAβ mice and non-transgenic littermates (NTL). (a) Twelve-month-old NTL. Small caliber vessels (CD31-positive endothelial cells: red) with Iba-1-positive (brown) perivascular macrophages (arrowhead) and Iba-1-positive (adjacent) inactive microglial cells (arrows). (b) Six-month-old arcAβ mouse. Small caliber vessels (CD31-positive endothelial cells: red) exhibit patchy Aβ deposition (blue, arrowheads). Staining for Iba-1 (brown) highlights the inactive microglial cells with their slender processes (short arrows) and the flatter perivascular macrophages (long arrow). (c) to (h) Twelve-month-old arcAβ mouse. (c) Small caliber vessels with CAA changes on a HE stain. One vessel exhibits homogenous eosinophilic thickening of the wall (*) due to Aβ deposition. On a more severely affected vessel, the eosinophilic material spreads out into the adjacent parenchyma (arrowheads), where activated microglial cells (arrows) are seen. (d) Triple staining of CD31, Aβ, and Iba1 confirms the deposition of Aβ (blue) in the vessel walls (CD31-positive endothelial cells: red), often circular over a stretch of a vessel (arrowheads), and with an occasional apposed activated microglial cell (arrows). (e) Closer view of affected vessels on the CD31/Aβ/Iba1 triple stain, with Aβ stretching from the vessel wall into the adjacent parenchyma (arrowheads) and closely apposed activated microglial cells (arrows). (f) Parenchymal Aβ plaque. Left: The Aβ plaque is represented on the HE stain by dense amorphous eosinophlic material (*) which is surrounded by cells with the morphology of activated microglia (arrows). Right: The CD31/Aβ/Iba1 triple stain reveals that the eosinophilic material represents Aβ (blue) and highlights the morphology of the associated activated microglial cells with Iba-1 (brown, arrows). (g) Focus with a few small caliber vessels with Perls' Prussian blue positive, iron laden perivascular macrophages (arrows) and scattered iron laden macrophages in the parenchyma (arrowhead). Inset: Double stain for iron (Perls' Prussian blue) and Iba-1 (brown) confirms the iron laden cells (arrows) as macrophages. Nuclear fast red counterstain. (h) In the DAB-enhanced Perls' stain, the shape of the iron-laden perivascular macrophages (arrows; inset: arrowheads) is better defined, and some positive cell processes stretching into the parenchyma can be seen (arrowheads). a, b, d–f (right): Triple immunohistology for Aβ (blue), Iba-1 (brown), and CD31 (red). Bars = 10 μm.

effect). This may amplify the R_2^* increase compared to magnetic susceptibility maps, which are largely devoid of blooming effects.

Histological analysis was performed to demonstrate the cellular uptake of USPIOs. We found that USPIOs target to CAA affected vessels with radii between 2 and 8 μm meaning that P904 accumulates at the microvasculature but not at larger cerebral vessels which is in a good agreement with the literature.[37,38] Although the actually measured radii of CAA affected vessels are lower than the radii of 10 to 40 μm reported previously which might be due to differences in the technical approaches,[18] the current study supports the finding that microvasculature is affected by the amyloid-induced vasculopathy.

In addition, we found that perivascular macrophages contained iron-positive material following injection of P904 in 12-month-old arcAβ mice whereas iron-containing cells in brain parenchyma were rarely seen (Figure 3(g) and (h), arrow heads). This confirms findings by Beckmann et al.[39] who detected iron oxide particles ingested by perivascular macrophages after intravenous injection in APP23 mice. Since, we have not seen morphological evidence of perivascular and parenchymal macrophage infiltration it is most likely that the residing perivascular macrophages have taken up P904 in situ.

Interestingly, Beckmann et al.[39] observed a mean number of 10 foci in the brain when assessing the 28-month-old APP23 mice with MRI, while we observed a much higher number of foci in arcAβ already at 12 months of age. This difference might be attributed to the different mouse strains but also to differences in the contrast agent. While Endorem, which was used in the study by Beckmann et al.,[39] is a SPIO particle with a hydrodynamic diameter of 150 nm, the hydrodynamic diameter of USPIO P904 is only 21 nm.[21] Although the uptake of Endorem by phagocytes is higher compared to P904 under in vitro conditions, the labeling efficiency may be reduced in vivo due to the shorter blood half-life of Endorem.[23]

Beckmann et al.[39] showed that iron oxide particle accumulation depends on the accumulation of vascular Aβ by comparing contrast agent accumulations in different mouse strains. While they observed only minor particle accumulation in the brains of PP23xPS45, APP24, and APP51 mice which show very little CAA, Endorem accumulated substantially in the brain of APP23 mice for which the degree of CAA was markedly higher. We have further analyzed the relationship between USPIO accumulation and CAA in the current study. In 6-month-old arcAβ mice, minimal vascular Aβ deposition was observed (Figure 3(b)), while in 12-month-old animals CAA was more pronounced (Figure 3(d) and (e)). We have previously shown that

CAA in arcAβ mice results in vascular remodeling with deposition of fibrinogen, loss of smooth muscle cells, blood–brain barrier impairment, and occurrence of cerebral microbleeds.[16–18] Surprisingly, we did not observe iron-positive perivascular macrophages around CAA-affected vessels but only around morphologically unaltered vessel without morphological evidence of CAA (Figure 3(g) and (h)). An explanation for this could be that in CAA-affected vessels, despite vascular remodeling, Aβ and fibrinogen deposition might physically prevent the USPIO from extravasating and thereby the uptake by tissue-resident macrophages. However, the fact that non-CAA-affected vessels show uptake of P904 indicates their increased permeability and thereby a functional vasculopathy. Using immunohistology, we observed activated microglia associated with vascular and parenchymal amyloid deposition. Activated microglia can change their microenvironment by secreting for example proangiogenic factors,[40] which in the vicinity of vessels might lead to blood–brain barrier impairment and thus extravasation of injected USPIO. We have found no evidence of Gd-DTPA leakage using dynamic contrast-enhanced MRI in arcAβ mice,[36] while blood–brain barrier damage has been described with histology in this mouse strain.[17] Hence, the USPIO-enhanced GRE MRI might provide a more sensitive read-out for vascular leakage in vivo than the dynamic contrast-enhanced MRI because of the cellular ingestion of particles by perivascular macrophages. The mechanisms of the functional impairment and their temporal dynamics are not known. The effect was clearly age-dependent as it was seen in 12-month-old but not in 6-month-old arcAβ mice. USPIO-enhanced GRE MRI provides a powerful non-invasive tool to study these vascular lesion loads during the disease course quantitatively, enabling a correlation with image-based read-outs of vascular dysfunction and thus shedding more light on the role of functional vasculopathy in the disease pathogenesis.

Declaration of conflicting interests

Authors' contributions

JK and AD conceived and designed the experiments. GDI, DK, MV, and AK performed the experiments. JK, AD, and AK analyzed the data. JK, AD, AK, JRR, and MR interpreted results. AS, FS, and JRR, contributed reagents/materials/analysis tools. JK, AD, and AK wrote the paper. All coauthors made critical revisions to the manuscript.

Supplementary material

Supplementary material for this paper can be found at http://jcbfm.sagepub.com/content/by/supplemental-data.

References

1. Bulte JW and Kraitchman DL. Iron oxide MR contrast agents for molecular and cellular imaging. *NMR Biomed* 2004; 17: 484–499.

2. Rad AM, Arbab AS, Iskander AS, et al. Quantification of superparamagnetic iron oxide (SPIO)-labeled cells using MRI. *J Magn Reson Imaging* 2007; 26: 366–374.

3. Kuhlpeter R, Danhke H, Matuszewski L, et al. R2 and R2* mapping for sensing cell-bound superparamagnetic nanoparticles: in vitro and murine in vivo testing. *Radiology* 2007; 245: 449–457.

4. Politi LS, Bacigaluppi M, Brambilla E, et al. Magnetic-resonance-based tracking and quantification of intravenously injected neural stem cell accumulation in the brains of mice with experimental multiple sclerosis. *Stem Cells* 2007; 25: 2583–2592.

5. Bowen CV, Zhang X, Saab G, et al. Application of the static dephasing regime theory to superparamagnetic iron-oxide loaded cells. *Magn Reson Med* 2002; 48: 52–61.

6. Muller RN, Gillis P, Moiny F, et al. Transverse relaxivity of particulate MRI contrast media: from theories to experiments. *Magn Reson Med* 1991; 22: 178–182.

7. Cantillon-Murphy P, Wald LL, Zahn M, et al. Measuring SPIO and Gd contrast agent magnetization using 3 T MRI. *NMR Biomed* 2009; 22: 891–897.

8. Dixon WT, Blezek DJ, Lowery LA, et al. Estimating amounts of iron oxide from gradient echo images. *Magn Reson Med* 2009; 61: 1132–1136.

9. McAuley G, Schrag M, Sipos P, et al. Quantification of punctuate iron sources using magnetic resonance phase. *Magn Reson Med* 2010; 63: 106–115.

10. Schäfer A, Wharton S, Gowland P, et al. Using magnetic field simulation to study susceptibility-related phase contrast in gradient echo MRI. *Neuroimage* 2009; 48: 126–137.

11. Schweser F, Deistung A, Lehr BW, et al. Quantitative imaging of intrinsic magnetic tissue properties using MRI signal phase: an approach to in vivo brain iron metabolism? *Neuroimage* 2011; 54: 2789–2807.

12. Schweser F, Sommer K, Deistung A, et al. Quantitative susceptibility mapping for investigating subtle susceptibility variations in the human brain. *Neuroimage* 2012; 62: 2083–2100.

13. Liu T, Spincemaille P, de Rochefort L, et al. Calculation of susceptibility through multiple orientation sampling (COSMOS): a method for conditioning the inverse problem from measured magnetic field map to susceptibility source image in MRI. *Magn Reson Med* 2009; 61: 196–204.

14. Liu T, Spincemaille P, de Rochefort L, et al. Unambiguous identification of superparamagnetic iron oxide particles through quantitative susceptibility mapping of the nonlinear response to magnetic fields. *Magn Reson Imaging* 2010; 28: 1383–1389.

15. Wong R, Chen X, Wang Y, et al. Visualizing and quantifying acute inflammation using ICAM-1 specific nanoparticles and MRI quantitative susceptibility mapping. *Ann Biomed Eng* 2012; 40: 1328–1338.

16. Klohs J, Deistung A, Schweser F, et al. Detection of cerebral microbleeds with quantitative susceptibility mapping in the ArcAbeta mouse model of cerebral amyloidosis. *J Cereb Blood Flow Metab* 2011; 31: 2282–2292.

17. Merlini M, Meyer EP, Ulmann-Schuler A, et al. Vascular β-amyloid and early astroctye alterations impair cerebrovascular function and cerebral metabolism in transgenic arcAβ mice. *Acta Neuropathol* 2011; 122: 293–311.

18. Klohs J, Baltes C, Princz-Kranz F, et al. Contrast-enhanced magnetic resonance microangiography reveals remodeling of the cerebral microvasculature in transgenic arcAβ mice. *J Neurosci* 2012; 32: 1705–1713.

19. Maat-Schieman ML, van Duinen SG, Bornebroek M, et al. Hereditary cerebral hemorrhage with amyloidosis-Dutch type (HCHWA-D): II—a review of histopathological aspects. *Brain Pathol* 1996; 6: 115–120.

20. Mandybur TI. The incidence of cerebral amyloid angiopathy in Alzheimer's disease. *Neurology* 1975; 25: 120–126.

21. Daldrup-Link HE, Golovko D, Ruffell B, et al. MRI of tumor-associated macrophages with clinically applicable iron oxide nanoparticles. *Clin Cancer Res* 2011; 17: 5695–5704.

22. Luciani A, Dechoux S, Deveaux V, et al. Adipose tissue macrophages: MR tracking to monitor obesity-associated inflammation. *Radiology* 2012; 263: 786–793.

23. Corot C, Port M, Guilbert I, et al. Superparamagnetic contrast agents. In: Modo MMJ and Bulte JWM (eds) *Molecular and cellular MR imaging*. Boca Raton, FL: CRC Press, 2007, pp.59–83.

24. López-Castro JD, Maraloiu AV, Delgado JJ, et al. From synthetic to natural nanoparticles: monitoring the biodegradation of SPIO (P904) into ferritin by electron microscopy. *Nanoscale* 2011; 3: 4597–4599.

25. Roemer PB, Edelstein WA, Hayes CE, et al. The NMR phased array. *Magn Reson Med* 1990; 16: 192–225.

26. Hammond KE, Lupo JM, Xu D, et al. Development of a robust method for generating 7.0 T multichannel phase images of the brain with application to normal volunteers and patients with neurological diseases. *Neuroimage* 2008; 39: 1682–1692.

27. Abdul-Rahman HS, Gdeisat MA, Burton DR, et al. Fast and robust three-dimensional best path phase unwrapping algorithm. *Appl Opt* 2007; 46: 6623–6635.

28. Wu B, Li W, Avram AV, et al. Fast and tissue-optimized mapping of magnetic susceptibility and T2* with multi-echo and multi-shot spirals. *NeuroImage* 2012; 59: 297–305.

29. Li W, Wu B and Liu C. Quantitative susceptibility mapping of human brain reflects spatial variation in tissue composition. *Neuroimage* 2011; 55: 1645–1656.

30. Miller AJ and Joseph PM. The use of power images to perform quantitative analysis on low SNR MR images. *Magn Reson Imaging* 1993; 11: 1051–1056.

31. McGibney G and Smith MR. An unbiased signal-to-noise ratio measure for magnetic resonance images. *Med Phys* 1993; 20: 1077–1078.

32. Ogawa S and Lee TM. Magnetic resonance imaging of blood vessels at high fields: in vivo and in vitro measurements and image simulation. *Magn Reson Med* 1990; 16: 9–18.

33. Wang H, De Rochefort L and Raynaud J. Quantitative susceptibility mapping applied to functionalized iron oxide nanoparticles in an Alzheimer's disease model. Presented at *ESMRMB 2012*, Lisbon, PT, 4–6 October, paper no. 399.

34. Stalder M, Phinney A, Probst A, et al. Association of microglia with amyloid plaques in brains of APP23 transgenic mice. *Am J Pathol* 1999; 154: 1673–1684.

35. Carare RO, Bernardes-Silva M, Newman TA, et al. Solutes, but not cells, drain from the brain parenchyma along basement membranes of capillaries and arteries: significance for cerebral amyloid angiopathy and neuroimmunology. *Neuropathol Appl Neurobiol* 2008; 34: 131–144.

36. Klohs J, Politano IW, Deistung A, et al. Longitudinal assessment of amyloid pathology in transgenic ArcAβ mice using multi-parametric magnetic resonance imaging. *PLoS One* 2013; 8: e66097.

37. Fischer VW, Siddiqi A and Yusufaly Y. Altered angioarchitecture in selected areas of brains with Alzheimer's disease. *Acta Neuropathol* 1990; 79: 672–679.

38. Miao J, Xu F, Davis J, et al. Cerebral microvascular amyloid beta protein deposition induces vascular degeneration and neuroinflammation in transgenic mice expressing human vasculotropic mutant amyloid beta precursor protein. *Am J Pathol* 2005; 167: 505–515.

39. Beckmann N, Gerard C, Abramowski D, et al. Noninvasive magnetic resonance imaging detection of cerebral amyloid angiopathy-related microvascular alterations using superparmagentic iron oxide particles in APP transgenic mouse models of Alzheimer's disease: application to passive Aβ immunotherapy. *J Neurosci* 2011; 31: 1023–1031.

40. Jantaratnotai N, Schwab C, Ryu JK, et al. Converging perturbed microvasculature and microglial clusters characterize Alzheimer disease brain. *Curr Alzheimer Res* 2010; 7: 625–636.